ORIGINAL ARTICLE

lajss.org
Latin American Journal of Solids and Structures

www.lajss.org

Characteristics of Stress Field Distribution during Elastoplastic Wave Transmission and Reflection in a Sandwich Bar System

Xie Chengjuan[a]*, Ren Wenke[b], Wu Yiding[b], Zhou Xuan[b], Gao Guangfa[b]*

[a] School of Mechanical Engineering, Nanjing University of Science and Technology, Nanjing, China. Emails: chengjuanxie@njust.edu.cn

[b] School of Mechanical Engineering, Nanjing University of Science and Technology, Nanjing, China. Emails: wenkeren@live.com, yidingwu@njust.edu.cn, zhoux@njust.edu.cn, gfgao@ustc.edu.cn

*Corresponding author

https://doi.org/10.1590/1679-78258030

Abstract

To study the propagation and evolution of one-dimensional elastoplastic waves within the system under rectangular, trapezoidal, and half-sine incident waves, leveraging elastoplastic incremental wave theory and numerical simulation calculations, the research qualitatively investigates the distribution and evolution of the stress field within the specimen, the impact of Bar 2 parameters, and the deformation characteristics of Bar 2 under these three types of incident waves. The findings indicate: Regardingthe overall stress uniformity of Bar 2 during the entire loading phase, the rectangular incident wave is the most effective, while the half-sine and trapezoidal waves are more advantageous for analyzing the stress conditions in Bar 2 during the early loading phase. The diameter and dimensionless density of the specimen significantly influence the stress non-uniformity, showing an approximate negative and positive correlation, respectively.

Keywords

SHPB, incident waveforms, stress field distribution, stress field evolution, Stress non-uniformity

Graphical Abstract

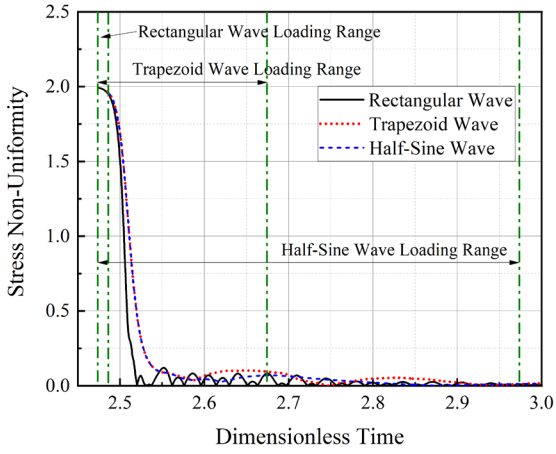

Received: February 07, 2024. In revised form: March 08, 2024. Accepted: March 08, 2024. Available online: March 19, 2024.
https://doi.org/10.1590/1679-78258030

1 INTRODUCTION

The Split Hopkinson Pressure Bar (SHPB) is an instrumental device for acquiring the dynamic mechanical behavior of materials under high strain rates (ranging from 10^2 to 10^4 s^{-1}). It has been extensively utilized for investigating the mechanical properties of materials under a uniaxial stress state. The SHPB outputs stress-strain curves parameterized by strain rates, thereby characterizing the constitutive response of materials under varying strain rates. The foundational principles and data processing schemes of the test rely on two fundamental assumptions: the uniaxial stress wave hypothesis and the uniformity of stress assumption (Gao, 2022). These underpinnings, however, impose numerous limitations on the experiment. The SHPB test, based on the theory of stress waves in solids, captures a wealth of information in the reflected and transmitted stress waves. This information, which includes insights into the specific state of the experimental setup, such as contact issues, bending of bars, coaxial problems (Prakash et al., 2023), and the dynamic properties of the specimen material, plays a crucial role in assessing the reliability of the experimental data. Consequently, precise analysis of waveforms and a thorough understanding of their formation, patterns, and mechanisms are essential prerequisites for refining SHPB experiments and data processing.

The current SHPB setup has been widely employed in studying the mechanical properties of materials, with many researchers endeavoring to enhance its accuracy. Significant progress has been made in this regard. Factors such as the incident wave shape, rise time, bar wave impedance, and the ratio of bar to specimen cross-sectional area all influence the stress equilibrium within the specimen. Employing a smooth incident wave, similar wave impedance between the bar and specimen, and a larger diameter of the specimen can improve the stress uniformity early stage within the specimen (Zhu et al., 2009). Moreover, analyzing the uniformity characteristics of stress under various waveforms based on the theory of uniaxial stress waves, and considering the effects of loading mode, generalized wave impedance ratio, and loading waveform on uniformity, it has been determined that rectangular wave loading is unsuitable for SHPB testing of any material (Li, and Shi-Sheng, 2005). The use of one-dimensional elastic wave theory reveals significant differences in stress uniformity and balance time sensitivity to relative wave impedance at different incident wave rise times (Yong-jian and Yu-long, 2008). Additionally, the impact of oblique loading pulses on early-stage stress uniformity shows that a gentler oblique wave results in quicker uniform stress distribution (Feng et al., 2010).

However, some core issues remain unresolved. Many experiments have not considered the axial stress non-uniformity when the wave impedance of the test material is high, nor have they considered the radial position's stress non-uniformity, leading to significant errors in the results (Dhahir and Marx, 2023; Jiao et al., 2023; Jin, et al., 2024; Shi et al., 2024; Platen et al., 2024; Zia et al., 2023). These factors have not received adequate attention and research. Indeed, while the SHPB test has developed rapidly, its underlying theory based on stress waves in solids has not been correspondingly propagated, leading to several issues in related experimental design and data analysis. The slow theoretical development of the SHPB test is a concern.

This article focuses on the so-called sandwich bar system in SHPB, comprising the incident bar, the specimen, and the transmission bar. Based on the time-varying stress at different locations in the elastoplastic incremental wave in solids, it studies the impact of various parameters of bar 2, such as diameter, dimensionless density, and plastic modulus, on the evolution of the stress field. It qualitatively describes the deformation characteristics of bar 2 under three typical incident waves; providing a process-based scientific basis for SHPB researchers to understand the distribution and evolution of the stress field. This research offers valuable reference for the design and data processing of SHPB experiments.

2 OVERVIEW OF THE SANDWICH BAR SYSTEM

The experimental setup, as depicted in Figure 1, resembles the Split Hopkinson Pressure Bar (SHPB) configuration, consisting of a sandwich bar system. This system includes three bars: Bar 1 with a length L_1 of 2000mm, the specimen (Bar 2) measuring 7.25mm in length L_2, and Bar 3 extending 1500mm in length L_3. Both Bar 1 and Bar 3 possess a diameter (D) of 14.5mm.

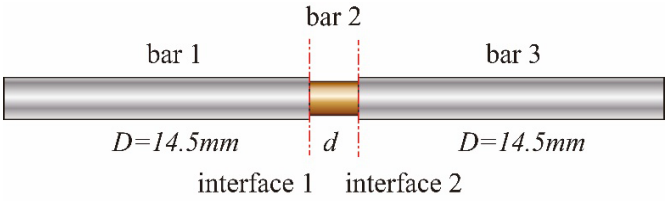

Figure 1 Schematic Diagram of a Quasi-One-Dimensional Sandwich Bar Structure.

All three bars share a uniform density ρ of 7.83g/cm^3. Bars 1 and 3 are composed of linear-elastic materials with a Young's modulus E^e of 210GPa and a Poisson's ratio of zero. Bar 2, the specimen, with a diameter (d) of 8mm, adheres to the bilinear model shown in Figure 2. This model is characterized by a yield strength Y of 200MPa, a plastic modulus E^p of 500MPa, and a Poisson's ratio of 0.29. Detailed specifications are provided in Table 1.

Table 1: Material Parameters of the Sandwich Bar System

Bar	E^e (GPa)	Y (MPa)	E^p (GPa)	Poisson's ratio	ρ (-g/cm^3)
Bar 1(3)	210	-	-	0	7.83
Bar 2	210	500	0.5	0	7.83

At the initial moment, a half-sine wave is applied to the left end face of Bar 1 in the system illustrated in Figure 1. This wave, with a wavelength λ of 800mm and a peak compressive strength of 250MPa, is depicted in Figure 3. The corresponding numerical simulation was conducted using ABAQUS/Explicit software, employing a two-dimensional axisymmetric geometric model (Minju et al., 2023). The geometric model, along with the parameters and material constitutive models, are consistent with the theoretical analysis.

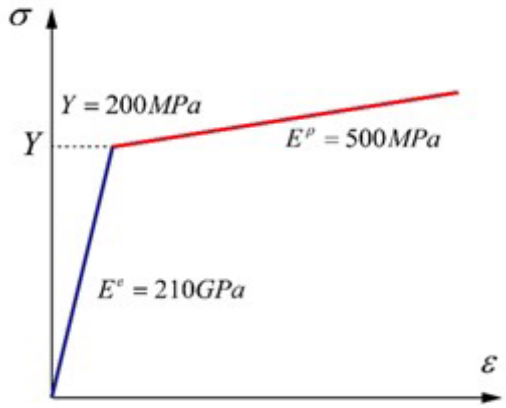

Figure 2 Schematic illustration of the Bilinear Constitutive Relationship

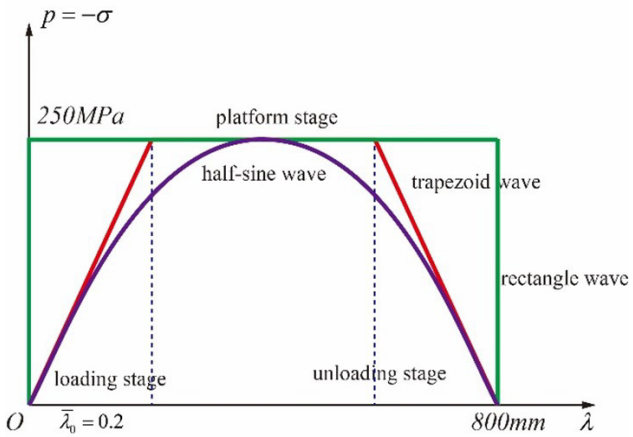

Figure 3 Three Typical Incident Compression Pulses.

The dimensionless time $\bar{t}$ and stress parameters $\bar{\sigma}$ are defined as follows:

$$\begin{cases} \bar{t} = \dfrac{t}{\lambda \Big/ \sqrt{E^e \Big/ \rho}} \\ \bar{\sigma} = \dfrac{\sigma}{-p} \end{cases} \tag{1}$$

The dimensionless time wavelength of the half-sine incident wave is set at 1, with a loading phase dimensionless time width of 0.5. The dimensionless stress ($\bar{\sigma}_I$) corresponding to the rising phase of the incident wave is:

$$\bar{\sigma}_I\left(\bar{t}\right) = -\sin\left(\pi\bar{t}\right) \tag{2}$$

For one-way propagation of a one-dimensional elastic wave in Bar 2, the required dimensionless time t_2^e is:

$$t_2^e = \frac{L_2 \Big/ \sqrt{E^e/\rho}}{\bar{t}} = 0.009 \tag{3}$$

In contrast, the dimensionless time (t_2^p) needed for a pure plastic wave is:

$$t_2^p = \frac{L_2 \Big/ \sqrt{E^p/\rho}}{\bar{t}} = 0.186 \tag{4}$$

Hence, the round-trip dimensionless time for an elastic wave in Bar 2 is approximately 0.018, while for a pure plastic wave, it is 0.371. The significantly shorter propagation time for the elastic wave implies that the first transmitted wave to reach Bar 2 will inevitably be elastic.

The generalized wave impedance ratios for Bar 2 during the elastic (k^e) and plastic (k^p) phases are:

$$\begin{cases} k^e = \dfrac{d^2}{D^2} \\ k^p = \sqrt{\dfrac{E^p}{E^e}} \cdot \dfrac{d^2}{D^2} \end{cases} \tag{5}$$

2.1 Determination of the Elastoplastic Transition Point C

Consider a loading wave where, at the instant point C reaches interface 1 and transmits to Bar 2, the average stress at the left end of Bar 2 precisely equals its yield stress. This moment is designated as the elastic-plastic transition point, with point C corresponding to a dimensionless intensity $\bar{\sigma}_T{}^C$ of:

$$\bar{\sigma}_T{}^C = \frac{Y}{-p} = 0.8 \tag{6}$$

To pinpoint the location of the elastic-plastic transition point, given that t_2^p is approximately 20 times as long as t_2^e, a preliminary setting for the dimensionless time interval is set at (0.018) across five points: points 1, 2, 3, 4, and point D, as shown in Figure 4. The dimensionless stress corresponding to point D is:

$$\bar{\sigma}_I{}^D = -\sin\left(\pi\bar{t}_{AD}\right) = -0.28088 \tag{7}$$

The incident wave can be divided into five equal time segments in Bar 2 according to the round-trip time of an elastic wave: segments A1, 12, 23, 34, and 4D. The dimensionless stresses corresponding to nodes 1 to 4 are -0.05691, -0.11364, -0.16999, and -0.22580, respectively. Thus, the dimensionless stress increments for these five segments are -0.05691, -0.05673, -0.05636, -0.05581, and -0.05507, detailed in Table 2.

Table 2: Dimensionless Stress of Each Bar Segment and Increment of Dimensionless Stress at Nodes

Bar 2	Nodes	Dimensionless Stress	Increment of Dimensionless Stress
A1	1	-0.05691	-0.05691
12	2	-0.11364	-0.05673
23	3	-0.16999	-0.05636
34	4	-0.22580	-0.05581
4D			-0.05507

The dimensionless stress values behind the transmitted wave at these five points upon reaching interface 1 are:

$$\begin{cases} \bar{\sigma}_1^{\,T} = \bar{\sigma}_{A1} \cdot T_\sigma^{\,e} \\ \bar{\sigma}_2^{\,T} = \left[\bar{\sigma}_{12} + \bar{\sigma}_{A1} \cdot F_\sigma^{\,e'}(2) \right] \cdot T_\sigma^{\,e} \\ \bar{\sigma}_3^{\,T} = \left[\bar{\sigma}_{23} + \bar{\sigma}_{12} \cdot F_\sigma^{\,e'}(2) + \bar{\sigma}_{A1} \cdot F_\sigma^{\,e'}(4) \right] \cdot T_\sigma^{\,e} \\ \bar{\sigma}_4^{\,T} = \left[\bar{\sigma}_{34} + \bar{\sigma}_{23} \cdot F_\sigma^{\,e'}(2) + \bar{\sigma}_{12} \cdot F_\sigma^{\,e'}(4) + \bar{\sigma}_{A1} \cdot F_\sigma^{\,e'}(6) \right] \cdot T_\sigma^{\,e} \\ \bar{\sigma}_5^{\,T} = \left[\bar{\sigma}_{45} + \bar{\sigma}_{34} \cdot F_\sigma^{\,e'}(2) + \bar{\sigma}_{23} \cdot F_\sigma^{\,e'}(4) + \bar{\sigma}_{12} \cdot F_\sigma^{\,e'}(6) + \bar{\sigma}_{A1} \cdot F_\sigma^{\,e'}(8) \right] \cdot T_\sigma^{\,e} \end{cases} \tag{8}$$

Here,

$$\begin{cases} T_\sigma^{\,e} = \dfrac{2k^e}{k^e+1} \dfrac{D^2}{d^2} = \dfrac{2}{k^e+1} = 1.5333 \\ F_\sigma^{\,e'}(n) = 1 + F_\sigma^{\,e'} + F_\sigma^{\,e'2} + \cdots + F_\sigma^{\,e'n} \end{cases}, F_\sigma^{\,e'} = \frac{1/k^e - 1}{1/k^e + 1} = \frac{1-k^e}{1+k^e} = 0.53327 \tag{9}$$

Similarly, the transmitted wave's post-stress for point 6, located a dimensionless time interval of 0.18 after point 5, is:

$$\bar{\sigma}_6^{\,T} = \left[\bar{\sigma}_{56} + \bar{\sigma}_{45} \cdot F_\sigma^{\,e'}(2) + \bar{\sigma}_{34} \cdot F_\sigma^{\,e'}(4) + \bar{\sigma}_{23} \cdot F_\sigma^{\,e'}(6) + \bar{\sigma}_{12} \cdot F_\sigma^{\,e'}(7) + \bar{\sigma}_{A1} \cdot F_\sigma^{\,e'}(10) \right] \cdot T_\sigma^{\,e} \tag{10}$$

The stress behind the transmitted wave at the instant when these six points on the incident wave reach Interface 1 is depicted in Figure 5.

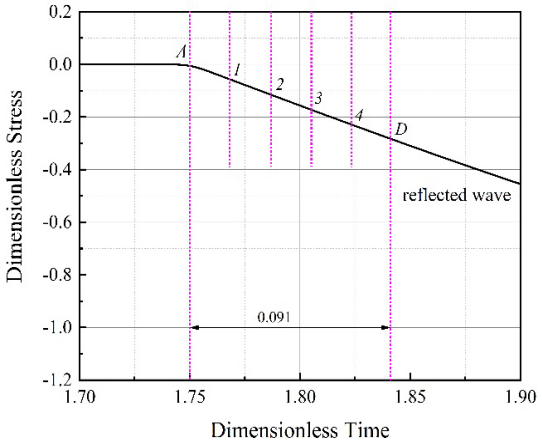

Figure 4 Incident Wave and Point D on It.

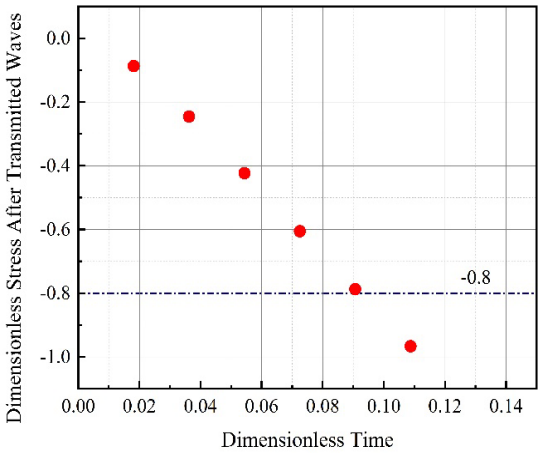

Figure 5 Dimensionless Stress Behind the Transmitted Wave at Six Points.

The stresses behind the transmitted waves at these six points on the incident wave, upon reaching interface 1, are depicted in Figure 5. From the figure, it is observable that the stress intensity behind the transmitted wave at point 5 is less than 0.8, while it exceeds 0.8 at point 6. Hence, the elastic-plastic transition point C on the incident wave is between points 5 and 6, closely approaching point 5. Therefore, we have:

$$\bar{\sigma}_T{}^C = \bar{\sigma}_{A1}{}^C + \bar{\sigma}_{12}{}^C + \bar{\sigma}_{23}{}^C + \bar{\sigma}_{34}{}^C + \bar{\sigma}_{45}{}^C + \bar{\sigma}_{5C}{}^C \tag{11}$$

Here,

$$\begin{cases} \bar{\sigma}_{A1}{}^C = \bar{\sigma}_{A1} \cdot T_\sigma{}^e \cdot F_\sigma{}^{e\prime}(10) \\ \bar{\sigma}_{12}{}^C = \bar{\sigma}_{12} \cdot T_\sigma{}^e \cdot F_\sigma{}^{e\prime}(8) \\ \bar{\sigma}_{23}{}^C = \bar{\sigma}_{23} \cdot T_\sigma{}^e \cdot F_\sigma{}^{e\prime}(6) \end{cases}, \begin{cases} \bar{\sigma}_{34}{}^C = \bar{\sigma}_{34} \cdot T_\sigma{}^e \cdot F_\sigma{}^{e\prime}(4) \\ \bar{\sigma}_{45}{}^C = \bar{\sigma}_{45} \cdot T_\sigma{}^e \cdot F_\sigma{}^{e\prime}(2) \\ \bar{\sigma}_{5C}{}^C = \bar{\sigma}_{5C} \cdot T_\sigma{}^e \end{cases} \tag{12}$$

The dimensionless time from point A to the elastic-plastic transition point C, the dimensionless intensities of the reflected and incident waves at point C, are:

$$\begin{cases} \bar{t}_{AC} = 0.092 \\ \bar{\sigma}_R{}^C = 0.07248 \\ \bar{\sigma}_I{}^C = -0.2846 \end{cases} \tag{13}$$

Figure 6 displays the time-course curve of dimensionless average stress on the left end face of Bar 2. Ignoring the viscous effects during simulation (Gao, 2023), which cause a curved transition at the wavefront, it is noted that approximately 0.092 units of dimensionless time later, the dimensionless average stress reaches -0.8, meeting the yield stress and aligning with theoretical calculations. Similarly, the dimensionless time width of the rising elastic segment of the reflected wave, as shown in Figure 7, is also approximately 0.092.

At this juncture, the dimensionless intensity of the incident wave at point C is -0.2846. Subsequently, the medium at the left end face of Bar 2, to the right of interface 1, enters a plastic state. When the incident wave reaches interface 1 post-point C, the interface is not purely elastic on both sides; the material in Bar 2 on the right is in a plastic state. At this point, the interface is considered an elastic-plastic interface, as illustrated in Figure 8.

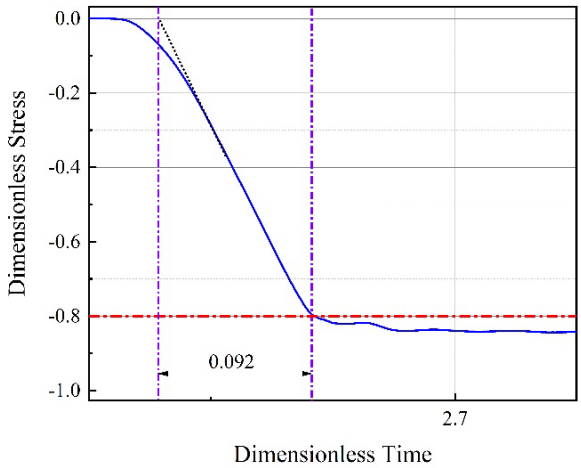

Figure 6 Time-Course Curve of Dimensionlszess Average Stress at the Left End of Bar 2.

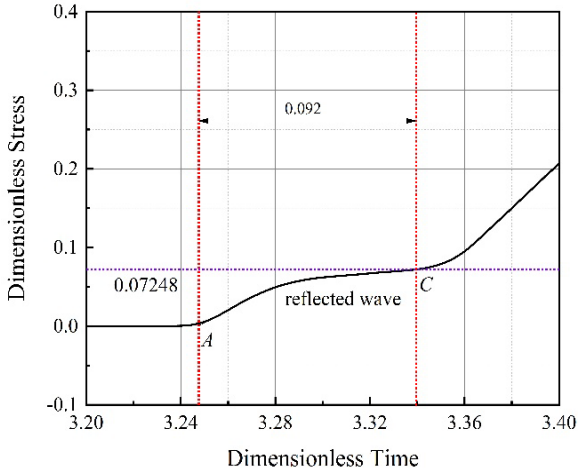

Figure 7 Dimensionless Time Width of the Elastic Segment of the Reflected Wave.

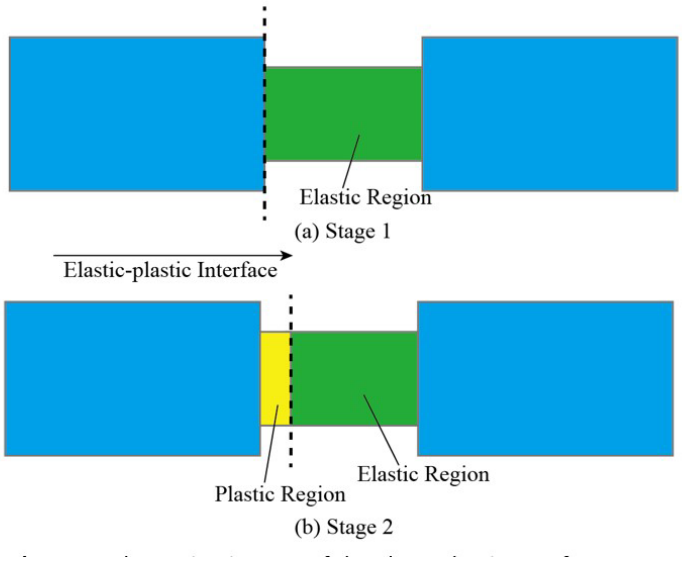

Figure 8 Schematic Diagram of the Elastoplastic Interface.

3 STRESS FIELD DISTRIBUTION AND EVOLUTION IN BAR 2 UNDER TYPICAL INCIDENT WAVES

Many experiments fail to consider the axial stress non-uniformity and radial stress disparities when testing materials with high wave impedances. These oversights often result in significant discrepancies in results, yet they have not received the attention and study they warrant. Thus, it becomes imperative to elucidate the actual stress field distribution and its evolution within the specimen in such sandwiched configurations, to identify the sources of error in the experiments.

3.1 Analysis of Dimensionless Stress Time-Course at Different Axial Positions

Comparing the reflected waves corresponding to three incident waves of identical intensity and wavelength, as shown in Figure 9, reveals distinct characteristics. The rectangular wave, due to its extremely short loading rise time, exhibits an indistinct transition between elasticity and plasticity. In contrast, the trapezoidal and half-sine waves, with their longer rise times, show a very clear elastic-plastic transition phase, with the half-sine wave being the most pronounced. Observing the reflected waves of these three types of incident waves, it is evident that with an increase in rise time, and due to a greater number of elastic reflections and transmissions within Bar 2, the stress at the elastic-plastic transition point C becomes smaller. This results in a greater stress intensity in the plastic loading segment of the incident wave. Since the absolute value of the reflection coefficient at the elastic-plastic interface 1 is significantly higher than that at a purely elastic interface, the half-sine wave appears above the trapezoidal wave, and the trapezoidal wave above the rectangular wave in the plateau or peak segment, as illustrated in Figure 9.

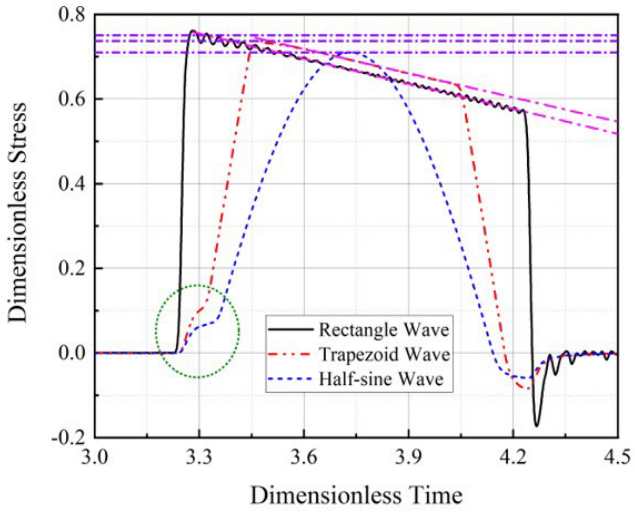

Figure 9 Characteristics of Reflected Waves Corresponding to Three Types of Incident Waves.

Figure 9 shows that when Bar 2's material is consistent and the diameter is uniformly 8mm, the reflected waves in Bar 1 under rectangular and trapezoidal wave incidents have a similar decay rate in the plateau phase. This observation aligns with theoretical analysis results: first, with Bar 2's material and size being consistent, the intensity of the plastic wave in Bar 2 and the transmission and reflection coefficients at both elastic-plastic interfaces should be consistent or similar. Therefore, the decay in reflected waves per unit time due to plastic wave transmission and reflection in Bar 2 is approximately the same. Second, as shown in Figure 10, although the maximum compressive engineering strain in Bar 2 under rectangular wave incident is greater than that under trapezoidal and half-sine waves, the slope of the compressive engineering strain increase over time is approximately the same. This means the compression and cross-sectional expansion per unit time in Bar 2 are nearly equal, resulting in a corresponding equivalence in the decay rate of the reflected wave due to cross-sectional expansion and the number of plastic wave transmissions and reflections. Combining these factors, the decay rates of reflected waves in Bar 1 under rectangular and trapezoidal wave incidents are approximately equal during the plateau phase.

However, regardless of whether the incident wave is rectangular, trapezoidal, or half-sine, the transmitted waveforms in Bar 3 are fundamentally similar and do not have a direct and noticeable correlation with the incident waveforms, as shown in Figure 11. The graph demonstrates that the dimensionless average stresses at the approximate beginning of the plateau phase for the transmitted waves corresponding to the three types of incident waves are all -0.244. However, the rectangular wave reaches the plateau phase quicker than the trapezoidal wave, which in turn is quicker than the half-sine wave. Moreover, during the plateau phase of the transmitted wave, the rate of stress increase for the three types of incident waves is approximately the same, as evidenced by the nearly parallel straight lines in Figure 11.

From Figures 9 and 11, it is apparent that the reflected and transmitted waves corresponding to the rectangular wave exhibit distinct oscillations at the start of the plateau phase, whereas the other two types of incident waves do not show such oscillations in their reflected waves.

Comparing the stresses at both ends of Bar 2 – the incident and transmission ends – under the three types of incident waves and considering the absolute value of the stress difference over time (as depicted in Figure 12), it is noticeable that in the early stages of the incident wave reaching Bar 2, the stress difference at both ends is significantly higher for the rectangular incident wave compared to the other two. The half-sine wave consistently shows the smallest stress difference at different times. The non-uniformity of stress at both ends of Bar 2 is defined as:

$$\delta_\sigma = \left| \frac{\sigma_1 - \sigma_2}{(\sigma_1 + \sigma_2)/2} \right| \tag{14}$$

where the subscripts 1 and 2 refer to the parameters at the left and right end faces of Bar 2, respectively. The time-course curves of stress non-uniformity at both ends of Bar 2 under the three types of incident waves are shown in Figure 13.

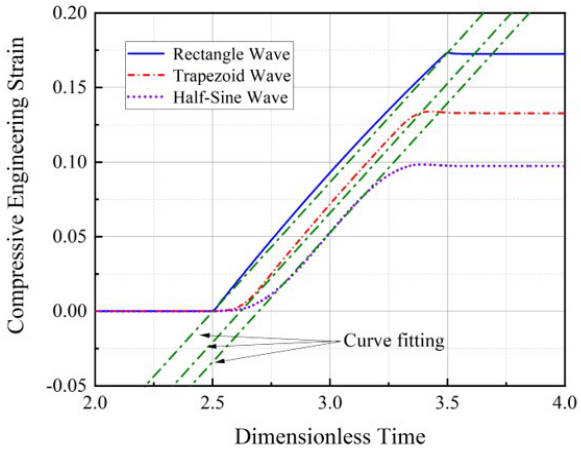

Figure 10 Engineering Strain Time-Course Curves for Three Types of Incident Waves with 8mm Diameter.

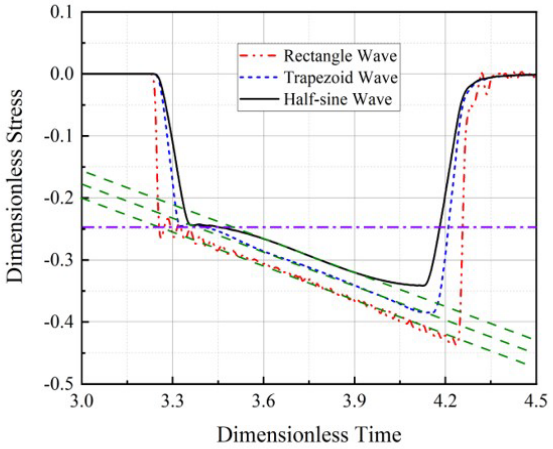

Figure 11 Characteristics of Transmitted Waves Corresponding to Three Types of Incident Waves.

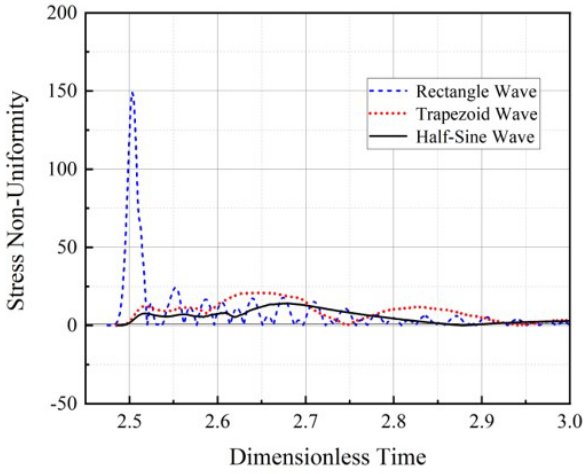

Figure 12 Absolute Values of Stress Difference for Three Types of Incident Waves with 8mm Diameter.

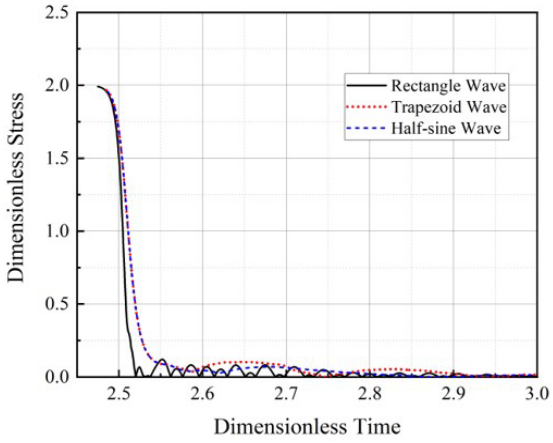

Figure 13 Stress Non-Uniformity for Three Types of Incident Waves with 8mm Diameter.

From the figure 14, it is evident that the rectangular wave reaches a relatively uniform state of stress more quickly compared to the other two types. However, it remains in a state of oscillation throughout; the trapezoidal and half-sine waves, after a rapid decline in the early stages, display a similar trend in their time-course curves, with the half-sine wave exhibiting the least stress non-uniformity, indicating better axial stress uniformity in Bar 2. It should be noted that although the stress non-uniformity under the rectangular wave declines quickly, due to its shorter loading time, the overall axial stress non-uniformity in Bar 2 remains high, close to 2. For the trapezoidal wave, the axial stress in Bar 2 becomes nearly uniform in the latter part of the loading phase. Analysis of the trapezoidal wave's transmission and reflection process in Bar 2 indicates an elastic loading time of approximately 0.062, suggesting that at a dimensionless time of 0.2 during the loading and plateau phases, the axial stress in Bar 2 is in a near-uniform state. As for the half-sine wave, Figure 13 shows that most of the loading phase in Bar 2 is in a near-uniform stress state. An analysis of the transmission and reflection process during the half-sine wave loading phase indicates an elastic interval dimensionless time width of 0.092, meaning that for approximately half the duration of elastic loading, the stress is in a near-uniform state.

Considering the dimensionless stress time-course curves at three axial positions in Bar 2 – the far left end, a quarter length from the left, and the axial center – as shown in Figures 15, 16, and 17, we observe distinct patterns. These figures respectively display the dimensionless stress time-course curves for the three nodes during rectangular wave incidence. A comparative analysis reveals: First, under the impact of all three types of incident waves, the nodal stress in Bar 2 rapidly reaches the plateau phase, exhibiting notable oscillatory characteristics in the early plateau phase before gradually stabilizing to a near-uniform axial stress; however, the oscillation amplitude is relatively larger and the frequency higher for the rectangular wave, with the half-sine wave showing the least oscillation. Second, the stress time-course curves at the axial center section of Bar 2 are the smoothest for all three types of incident waves. Third, although the oscillation in the early plateau phase is most pronounced for the rectangular wave, it also has the largest zone of relatively uniform and smooth stress, followed by the trapezoidal wave. The half-sine wave, due to its immediate unloading post-loading, has the least overlapping segments in the time-course curves of the three nodes, despite its overall good stress uniformity.

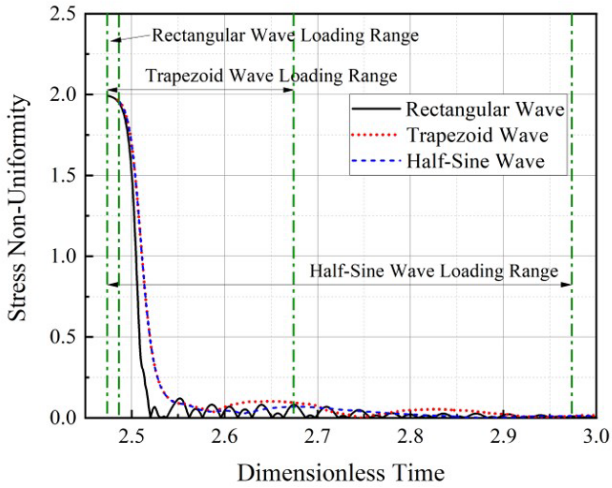

Figure 14 Stress Non-Uniformity in Different Sections for Three Types of Incident Waves.

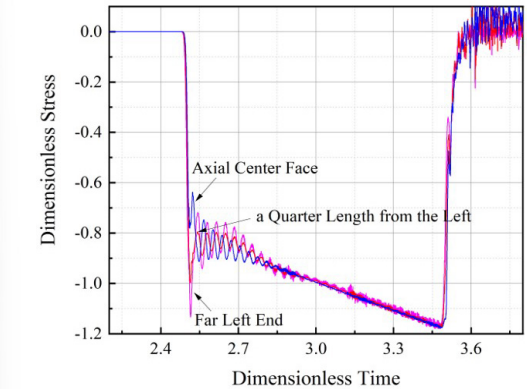

Figure 15 Stress Time-Course Curve Along the Axial Centerline of Bar 2 Under Rectangular Wave.

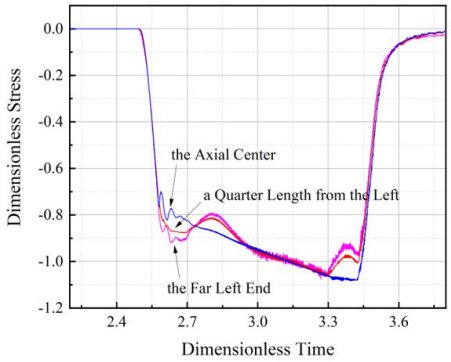

Figure 16 Stress Time-Course Curve Along the Axial Centerline of Bar 2 Under Trapezoidal Wave.

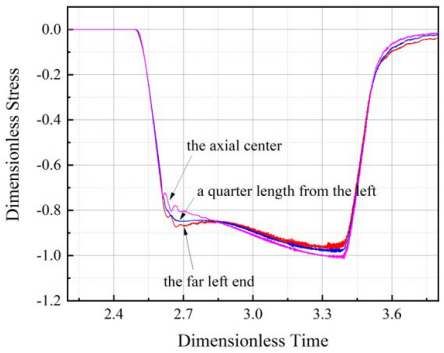

Figure 17 Stress Time-Course Curve Along the Axial Centerline of Bar 2 Under Half-Sine Wave.

When the incident wave reaches the left end of Bar 2 and propagates through it, the stress in the radial direction at different axial positions of Bar 2 is not uniform due to the mismatch in the areas of Bars 1, 3, and 2. Figure 18(a) illustrates the dimensionless stress time-course curves at the center point, outermost edge, and halfway radius of Bar 2's left end face under a rectangular wave incidence with a diameter of 8mm. Similar to the axial direction, the early plateau phase shows significant oscillations and notable stress differences at the same moments, which gradually diminish and even out over time, leading to an approximate convergence in the stress time-course curves of the three nodes.

3.2 Analysis of Dimensionless Stress Time-Course at Different Radial Positions

Figure 18(b) shows the time-course curves for three corresponding positions at the axial midpoint section, exhibiting characteristics similar to those at the left end face, but with significantly smaller stress differences across different radial positions, resulting in less pronounced oscillations for the nodes.

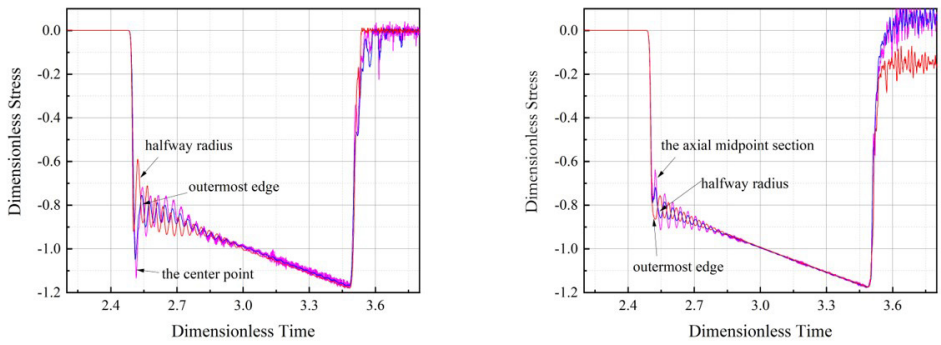

（a）*the Left End Face*　　（b）*Axial Midpoint Cross-Section*

Figure 18 Stress Time-Course Curves at Different Radial Positions on the Cross-Section of Bar 2 Under Rectangular Wave.

For trapezoidal wave incidence, the left end face node stress oscillations are larger but with a lower frequency, and oscillations also appear in the later stages of the plateau phase, as shown in Figure 19. However, at the axial midpoint section, the node stress oscillation intervals are noticeably shorter compared to the rectangular wave incidence, with better overlapping of the stress time-course curves across different radial positions.

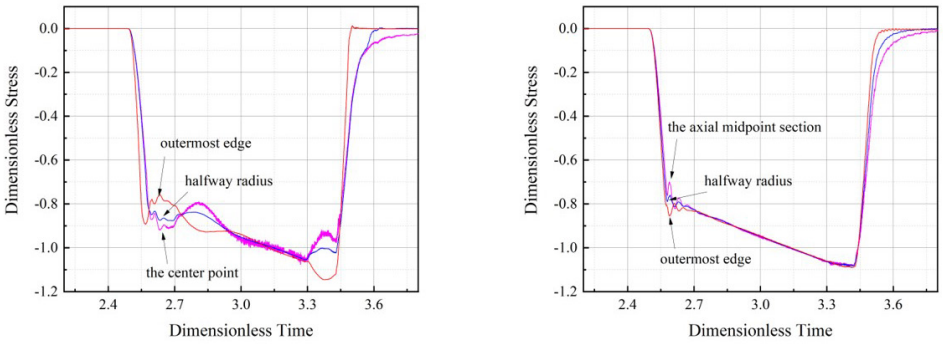

(a) *the Left End Face*　　（b）*Axial Midpoint Cross-Section*

Figure 19 Stress Time-Course Curves at Different Radial Positions on the Cross-Section of Bar 2 Under Trapezoidal Wave.

The stress time-course curves for the half-sine wave at both sections are similar to those for the trapezoidal wave, as illustrated in Figure 20.

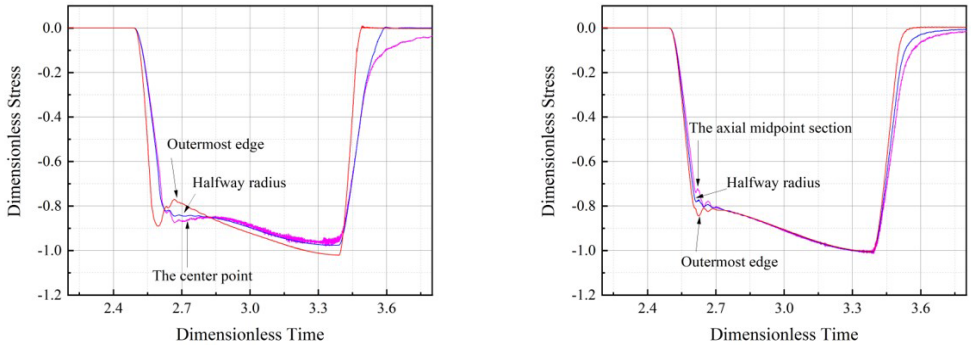

（a）*the Left End Face*　　（b）*Axial Midpoint Cross-Section*

Figure 20 Stress Time-Course Curves at Different Radial Positions on the Cross-Section of Bar 2 Under Half-Sine Wave.

Comparing the three types of incident waves across Figures 18, 19, and 20, it is evident that in terms of overall stress uniformity in Bar 2 during the entire loading phase, the rectangular wave performs best. However, for analyzing the stress conditions in Bar 2 during the early loading phase, the half-sine and trapezoidal waves are more advantageous.

4 INFLUENCE OF BAR 2 PARAMETERS ON STRESS FIELD EVOLUTION

In the foundational theory of the Split Hopkinson Pressure Bar (SHPB), parameters like the generalized impedance and specimen diameter, especially for heterogeneous materials such as concrete, are of crucial importance. Hence, this chapter delves into an analysis of specimen diameter, dimensionless density, and plastic modulus.

4.1 Impact of Specimen Diameter on Stress Field Evolution

Figure 21 illustrates the time-course curves of stress non-uniformity at both ends of Bar 2 under the impact of three different incident waves, with diameters ranging from 14.5mm to 4mm. It is observed that regardless of the type of incident wave – be it rectangular, trapezoidal, or half-sine – the stress non-uniformity reaches a relatively uniform interval quickest when Bar 2's diameter is 4mm. However, as the diameter increases, the dimensionless time required also increases. Nonetheless, this doesn't imply that a smaller diameter directly correlates with a smaller stress difference at both ends of Bar 2. As the diameter decreases, the axial dimensionless stress in the bar increases, enlarging the denominator in the expression for stress non-uniformity in Equation (2), thus gradually reducing the corresponding stress non-uniformity for the same stress difference.

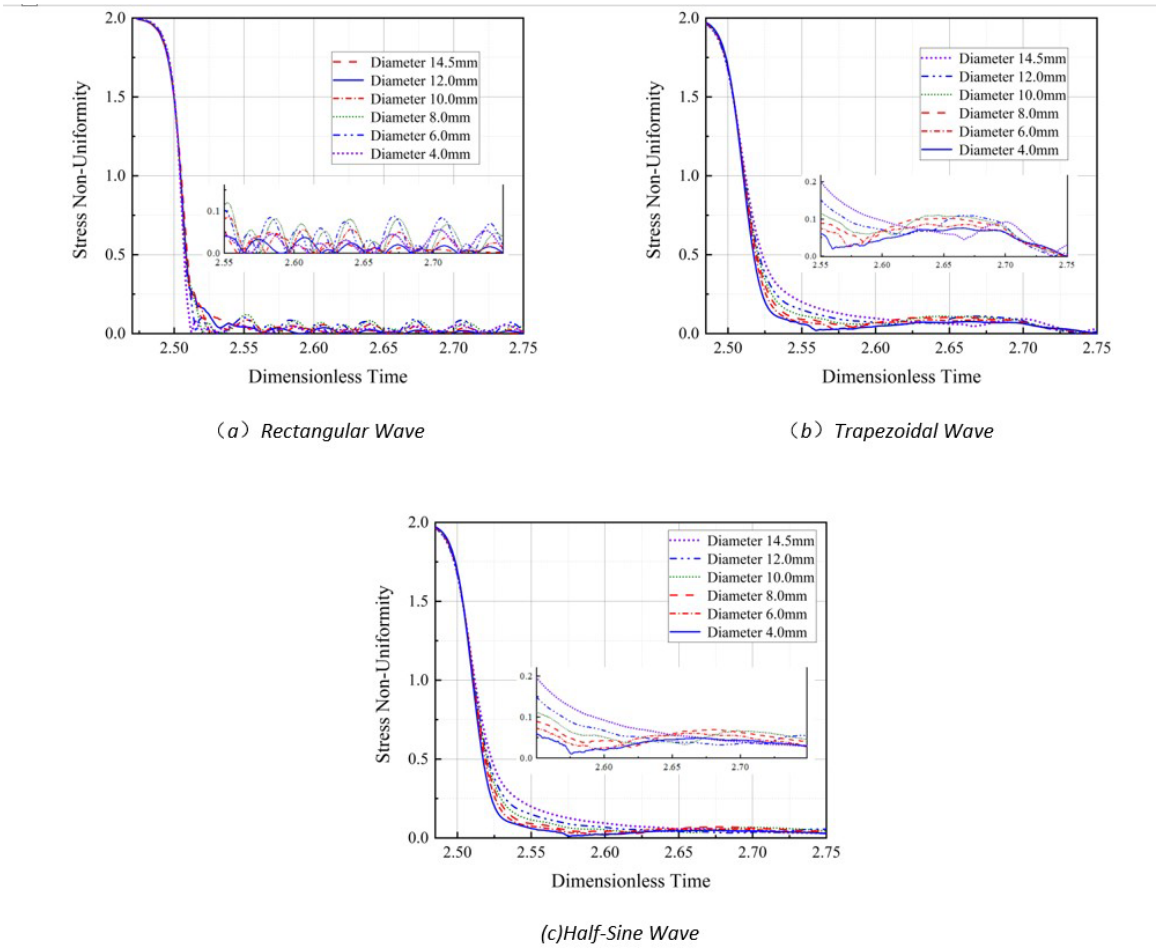

Figure 21 Stress Non-Uniformity at Both Ends of Bar 2 Under Three Types of Incident Waves with Different Diameters.

In fact, as evident from Figure 22, which shows the time-course curves of axial dimensionless stress in Bar 2 with diameters of 4mm and 12mm, the axial stress associated with a diameter of 12mm exhibits significantly less local oscillation and overall fluctuation compared to the 4mm diameter. Particularly in the early plateau phase, the stress oscillations at 4mm are markedly higher than those at 12mm. A comparison of the subfigures in Figure 21 reveals that, for the rectangular wave, different Bar 2 diameters lead to relatively high-frequency oscillations upon reaching a stable phase of stress non-uniformity. In contrast, for trapezoidal and half-sine waves, the oscillation frequency is notably lower, especially for the half-sine wave, where the stress non-uniformity time-course curve is exceptionally smooth and stable.

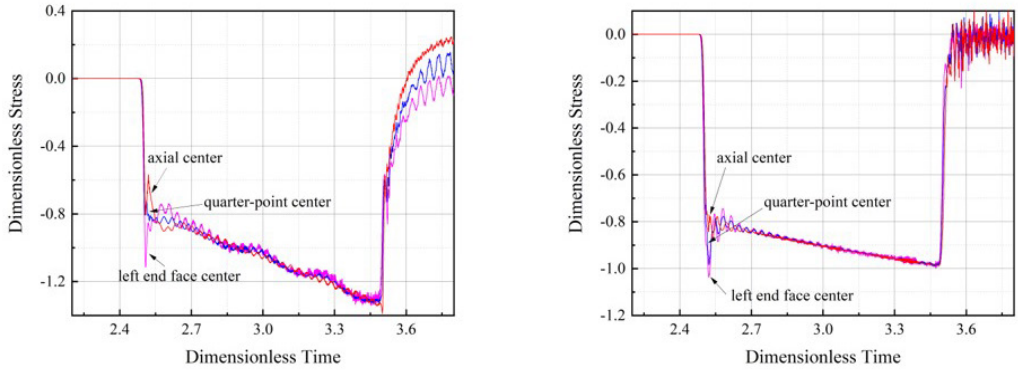

（a）4mm （b）12mm

Figure 22: Stress Time-Course Curves at Different Axial Positions on the Cross-Section of Bar 2 with Varying Diameters Under Rectangular Wave.

Figure 22 also depicts noticeable stress disturbances in the early plateau phase, primarily due to two factors: the dispersion effect caused by radial inertia as a result of Poisson's ratio of 0.5 during the plastic phase, and the substantial difference in forces at different radial positions on the cross-section near the contact ends due to mismatched cross-sectional areas of Bar 2 and the other two bars. In the later stages, as Bar 2 entirely enters the plastic state, minor variations in radial position strains lead to reduced stress non-uniformity and an appearance of gradual uniformity; moreover, the stress distribution uniformity at the axial center section of Bar 2 is significantly better compared to the left end face section.

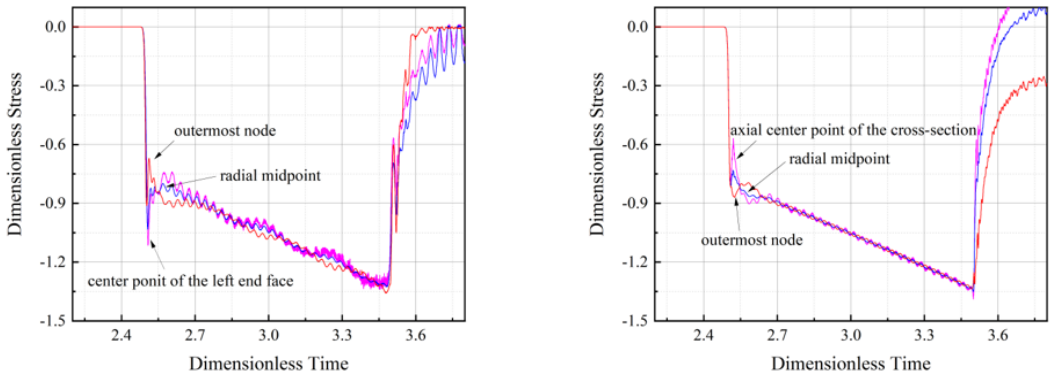

（a）the Left End Face （b）Axial Midpoint Cross-Section

Figure 23 Stress Time-Course Curves at Different Radial Positions on the Cross-Section of Bar 2 with 4mm Diameter Under Rectangular Wave.

As the diameter of Bar 2 decreases, the stress distribution non-uniformity across different radial positions on the same cross-section becomes more pronounced. Figure 23 presents the dimensionless stress time-course curves at three different radial positions on the left end face and axial center section of Bar 2 with a diameter of 4mm. Comparing Figures 23 and 24, it is evident that there are similar patterns between the two, but the stress non-uniformity is more pronounced when Bar 2's diameter is 4mm due to worse area matching. This is especially noticeable on the left end face, as shown by comparing Figures 23(a) and 24(a), where the former demonstrates less ideal stress uniformity throughout the plateau phase.

4.2 Influence of Specimen Dimensionless Density on Stress Field Evolution

Assuming a diameter of 8mm for Bar 2 and considering a gradual decrease in the material's dimensionless density from 1 to 1/6, the time-course curve of stress non-uniformity at both ends of Bar 2 under a rectangular incident wave is displayed in Figure 25(a). The figure shows that when the dimensionless density of Bar 2's material reduces from 1/2 to 1/6, the stress non-uniformity time-course curves largely coincide without significant differences, while the curve for dimensionless density 1 differs from the others.

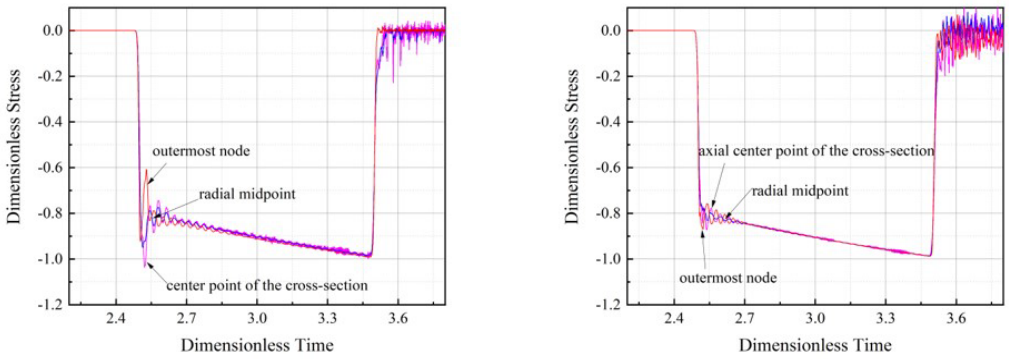

（a）*the Left End Face* （b）*Axial Midpoint Cross-Section*

Figure 24 Stress Time-Course Curves at Different Radial Positions on the Cross-Section of Bar 2 with 12mm Diameter Under Rectangular Wave.

Moreover, Figure 25(a) reveals that after the stress non-uniformity reaches zero for the first time, it continues to oscillate. Notably, the oscillation amplitude does not follow a monotonic decreasing trend but alternates, with the 1st, 3rd, 5th, etc., oscillations showing a decreasing trend, and the 2nd, 4th, 6th, etc., oscillations also decreasing monotonically.

In contrast to the rectangular incident wave, the trapezoidal wave's impact on the stress non-uniformity time-course curve is significantly more pronounced. Firstly, due to the trapezoidal wave's longer elastic loading time compared to the rectangular wave, and the increased speed of elastic waves at lower dimensionless densities, the elastic wave travels back and forth multiple times in Bar 2 before the elastic-plastic transition point of the incident wave reaches Interface 1. This results in a rapid decrease in stress non-uniformity at both ends of Bar 2 during the elastic phase. Additionally, as the dimensionless density decreases, the stability of the stress non-uniformity after first reaching a relatively uniform state improves, with a smaller and nearly constant stress non-uniformity, and the curves are smoother without the noticeable oscillations characteristic of the rectangular wave, as seen in Figure 25(b).

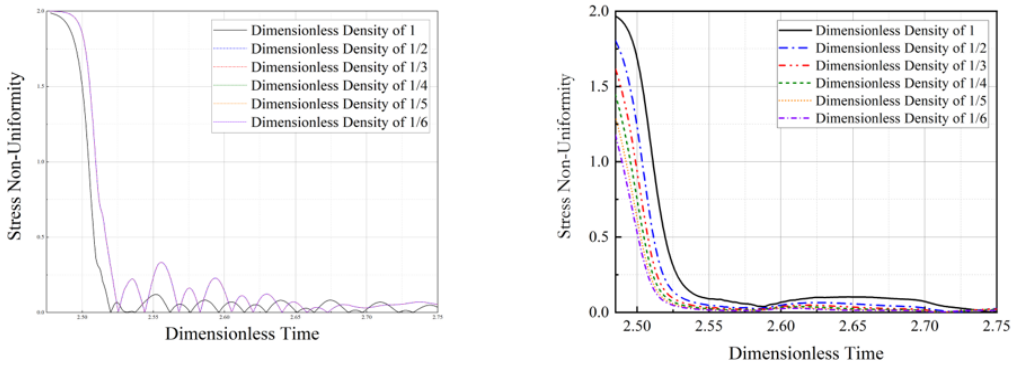

（a）*Rectangle Wave* （b）*Trapezoid Wave*

Figure 25 Stress Non-Uniformity Time-Course Curves for Bar 2 with Different Dimensionless Densities Under Rectangular and Trapezoidal Waves.

4.3 Effect of Specimen Plastic Modulus on Stress Field Evolution

In the foundational theory of the Split Hopkinson Pressure Bar (SHPB), certain parameters, such as the specimen's plastic modulus, are pivotal, especially when it is varied from 500 MPa to 100 MPa while keeping other material parameters of Bar 2 constant. It is observed that under both rectangular and trapezoidal incident waves, the stress non-uniformity on the end faces of Bar 2 approximately coincides. However, as dimensionless time increases, slight differences begin to emerge among the time-course curves for different plastic moduli, as illustrated in Figure 26. Moreover, since the rapid decrease in stress non-uniformity during the initial phase of the incident wave is primarily caused by the elastic wave's transmission and reflection within Bar 2, the impact of the plastic wave becomes negligible.

Consequently, the influence of the plastic modulus also diminishes, leading to a theoretical overlap in the stress non-uniformity time-course curves for any type of incident wave under unchanged conditions other than the plastic modulus.

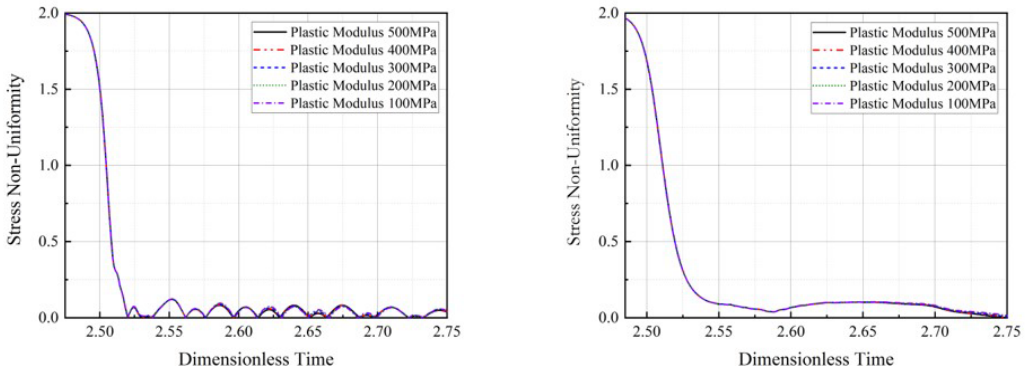

Figure 26 Stress Non-Uniformity Time-Course Curves for Bar 2 with Different Plastic Moduli Under Rectangular and Trapezoidal Waves.

5 DEFORMATION CHARACTERISTICS OF BAR 2 UNDER THREE TYPICAL INCIDENT WAVES

Taking the half-sine incident wave as an example, a comparison of the time-course curves for compressive engineering strain at different diameters of Bar 2 reveals that as the diameter increases, the compressive engineering strain at any given moment decreases, as depicted in Figure 27. Comparing the time-course curves of compressive engineering strain for the three types of incident waves, it is evident that at the same diameter, the strain value for the rectangular wave is significantly higher than that for the trapezoidal wave, which in turn is markedly greater than that for the half-sine wave, as shown in Figure 28.

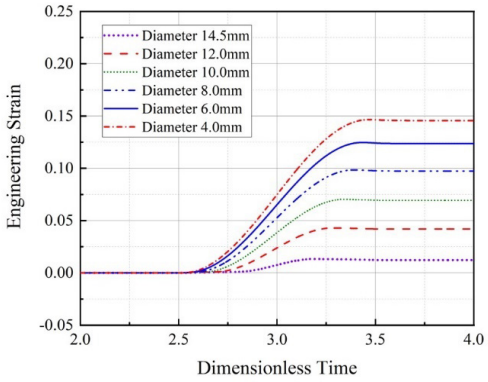

Figure 27 Engineering Strain Under Half-Sine Wave with Different Diameters of Bar 2.

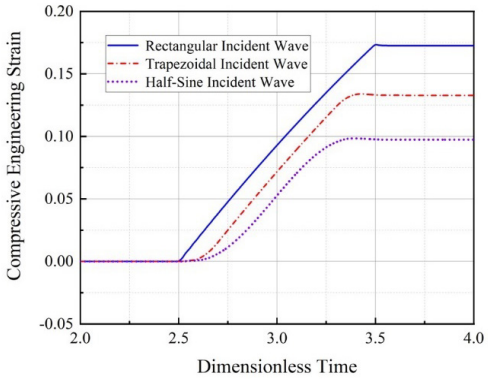

Figure 28 Engineering Strain for Different Incident Waves with 8mm Diameter Bar 2.

Given that the Young's modulus of Bar 2's material, at 210 GPa, is substantially higher than its plastic modulus of 500 MPa (420 times higher), the compressive engineering strain during the elastic phase can be disregarded. When considering an ideal rectangular wave, if we ignore the distinction between engineering stress and true stress, as well as engineering strain and true strain, the plastic work per unit time increases in an approximately linear fashion until the incident energy is exhausted. In reality, as shown in Figure 28, this near-linear increase should form a slightly convex curve, considering that true stress increases with increasing compressive engineering strain. With a trapezoidal wave, the incident energy during the rising and plateau phases is notably less than that of a rectangular wave, resulting in a lower total strain value. However, during the plateau phase, the unit strain energy absorption is similar to that of a rectangular wave, hence the slope of the compressive engineering strain time-course curve during this phase is comparable to that of a rectangular wave, as illustrated in Figure 28. For a half-sine wave, the incident energy is the least, especially during the loading phase, leading to the smallest total strain value.

Figure 29 presents the maximum compressive engineering strain values under the impact of three different incident waves for varying diameters of Bar 2. It is observed that with increasing diameter, the maximum strain value for each type of incident wave decreases in an approximately linear manner, with the rate of decrease being fastest for the rectangular wave and slowest for the half-sine wave.

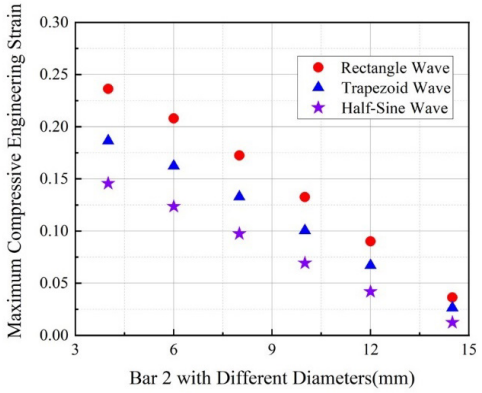

Figure 29 Engineering Strain for Bar 2 with Different Diameters.

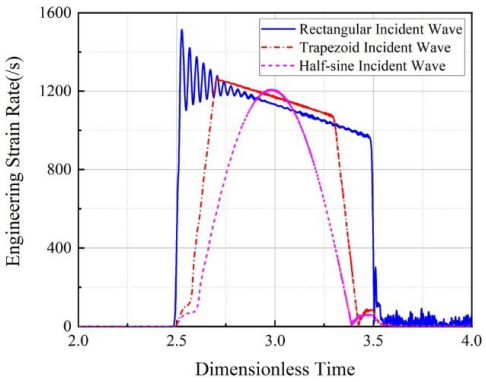

Figure 30 Engineering Strain Rate Time-Course Curves for Three Types of Incident Waves with 8mm Diameter Bar 2.

In contrast to the characteristics of Bar 2's strain time-course curves under different incident waves, which are similar but with notable peak differences, the characteristics of Bar 2's compressive engineering strain rate time-course curves are closely related to the incident waves. Specifically, the shape of the compressive engineering strain rate time-course curve mirrors the reflection wave within Bar 2, as shown in Figure 30.

Furthermore, as the diameter of Bar 2 increases, the characteristics of its compressive engineering strain rate also resemble the deformation features of the reflected wave in Bar 1. However, the oscillation amplitude of the strain rate time-course curve is notably larger compared to the reflected wave, as demonstrated in Figures 31 to 33.

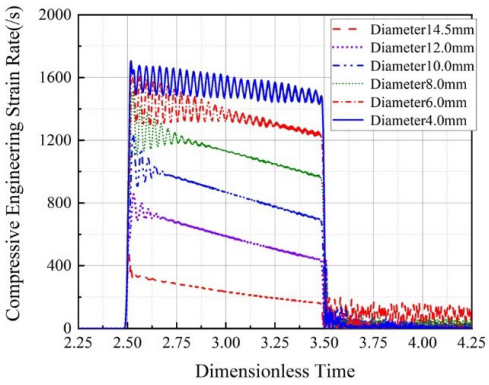

Figure 31 Engineering Strain Rate Time-Course Curve Under Rectangular Wave with Different Diameters of Bar 2.

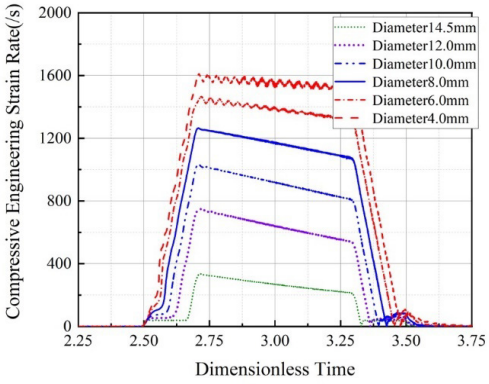

Figure 32 Engineering Strain Rate Time-Course Curve Under Trapezoidal Wave with Different Diameters of Bar 2.

As observed in Figure 31, with the increase in diameter of Bar 2, the oscillatory region of the engineering strain rate time-course curve gradually diminishes, specifically, the endpoint of the oscillation region moves forward. Figure 32 exhibits a similar pattern. Comparing Figures 31, 32, and 33, it is evident that for the same diameter, the engineering strain rate time-course curve corresponding to the half-sine wave is smoother than that of the trapezoidal wave, both of which are significantly smoother than the curve during the rectangular wave incidence.

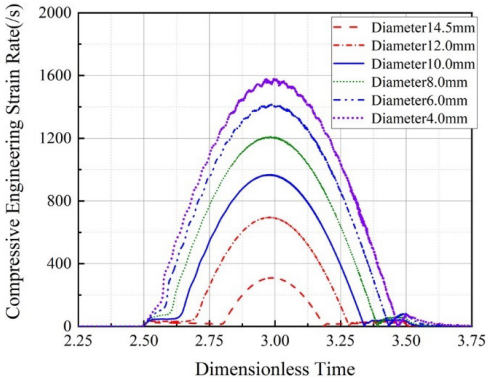

Figure 33 Engineering Strain Rate Time-Course Curve Under Half-Sine Wave with Different Diameters of Bar 2.

6 CONCLUSION

In the context of the SHPB test's sandwich bar system, leveraging the theory of elastoplastic incremental waves combined with numerical simulation calculations, a quantitative investigation is conducted on the propagation and

evolution of one-dimensional elastoplastic waves in the system under rectangular, trapezoidal, and half-sine incident waves, the influence of Bar 2 parameters, and the deformation characteristics of Bar 2 under the impact of these three types of incident waves:

Under the impact of rectangular and trapezoidal incident waves, the decay rates of the reflected waves in Bar 1 during the plateau phase are approximately equal. In contrast to Bar 1's reflected waves, the transmitted waveforms in Bar 3 are fundamentally similar regardless of the incident wave type, showing no direct correlation with the shape of the incident waves. The rectangular wave reaches a relatively uniform stress state more rapidly compared to the other two types. In the initial rapid decline phase of stress non-uniformity, the time-course curves for the trapezoidal and half-sine waves largely coincide, with the half-sine wave exhibiting the best axial stress uniformity in Bar 2 post this rapid decline. For all three types of incident waves, the stress time-course curve at the axial center section of Bar 2 is the smoothest compared to the other positions along the axial centerline.

The difference in stress at various radial positions on the axial midpoint cross-section of Bar 2 is significantly smaller. For the trapezoidal and half-sine incident waves, the oscillation interval of node stress at the left end face is larger but with a lower frequency, and the oscillation interval of node stress on the axial midpoint cross-section is notably shorter compared to the rectangular incident wave, with better congruence in the stress time-course curves across different radial positions. Hence, in terms of the overall stress uniformity of Bar 2 during the entire loading phase, the rectangular incident wave is relatively the best option, while for analyzing the stress conditions in Bar 2 during the early loading phase, the half-sine and trapezoidal waves are more beneficial.

As the diameter of Bar 2 changes, from 14.5mm to 4mm, regardless of the incident wave type, the stress non-uniformity at both ends of Bar 2 with a 4mm diameter reaches a relatively uniform interval fastest, and the stress distribution non-uniformity across different radial positions on the same cross-section becomes more pronounced. With a diameter of 8mm and a gradual reduction in the dimensionless density of Bar 2's material from 1/2 to 1/6, the stress non-uniformity time-course curves under a rectangular incident wave largely coincide, while the curve for dimensionless density 1 shows differences from those of the other five densities. Moreover, when the plastic modulus of Bar 2's material is reduced from 500MPa to 100MPa, with other parameters remaining constant, the stress non-uniformity at both ends of Bar 2 is nearly identical for both rectangular and trapezoidal incident waves. Only as the dimensionless time increases do minor differences begin to emerge in the time-course curves between different plastic moduli.

When the incident wave is a half-sine wave, an increase in the diameter of Bar 2 results in a reduction in the engineering strain at the same moment. For the same diameter, the engineering strain due to a rectangular incident wave is significantly higher than that caused by a trapezoidal wave, which in turn is greater than that induced by a half-sine wave.

ACKNOWLEDGMENTS

The author(s) disclose the receipt of the following financial support for the research, authorship, and/or publication of this article: The project was supported by the National Natural Science Foundation of China (Grant No: 12172179, U2341244, 11772160).

Author's Contributions: Conceptualization, XIE Chengjuan and ZHOU Xuan; Methodology, REN Wenke; Investigation, ZHOU Xuan, WU Yiding and GAO Guangfa; Writing - original draft, XIE Chengjuan, REN Wenke and GAO Guangfa; Writing - review & editing, GAO Guangfa; Funding acquisition, GAO Guangfa; Resources, WU Yiding and XIE Chengjuan; Supervision, GAO Guangfa.

Editor: Marcílio Alves

References

Dhahir, Mohammed K., and Steffen Marx. (2023). "Development of expansive concrete for chemical prestressing applications." Case Studies in Construction Materials 19: e02611.

Feng, Ping, et al. (2010). "Influence of incident pulse of slope on stress uniformity and constant strain rate in SHPB test." Transactions of Beijing institute of Technology 5: 513-516.

Gao G. (2022). "Introduction to Stress Waves in Solid." Beijing: Science Press.

Gao G. F. (2023). “Meticulous Analysis of One-Dimensional Elastic-Plastic Wave Evolution in Sandwich Bar System (Part I): Transmitted and Reflected Waves for Typical Loading Waves. ” Explosion and Shock Waves.

Jiao, Run-Hao, Feng, De-Cheng, Shen, Lei, and Gang Wu. 2023. “A confined concrete model considering strain gradient effect of CFST column under eccentric load.” Structures. 58: 105645.

Jin, Libing, et al. (2024). “Carbon-footprint based concrete proportion design using LSTM and MOPSO algorithms.” Materials Today Communications 38: 107837.

Li, Song, and H. U. Shi-Sheng. (2005). “Stress uniformity and constant strain rate in SHPB test.” Explosion and Shock Waves 25.3: 207-216.

Minju, Qi, et al. (2023). “Analysis of Stress, Strain and Young's Modulus of Specimens under Propagation of the 1D Linear Elastic Stress Waves.” Latin American Journal of Solids and Structures 20: e513.

Platen, Jakob, et al. (2024). “The microlayer model: A novel analytical homogenisation scheme for materials with rigid particles and deformable matrix-applied to simulate concrete.” Computers & Structures 293: 107258.

Prakash, Gyan, N. K. Singh, and N. K. Gupta. (2023). “Flow behaviour of Ti-6Al-4V alloy in a wide range of strain rates and temperatures under tensile, compressive and flexural loads.” International Journal of Impact Engineering 176: 104549.

Shi, Jing, et al. (2024). “Experimental evaluation of fracture toughness of basalt macro fiber reinforced high performance lightweight aggregate concrete.” Construction and Building Materials 411: 134638.

Yong-jian, M. A. O., and L. I. Yu-long. (2008). “Axial stress uniformity in specimens of SHPB tests.” Explosion And Shock Waves 28.5: 448-454.

Zhu, Jue, Shisheng Hu, and Lili Wang. (2009). “An analysis of stress uniformity for concrete-like specimens during SHPB tests.” International Journal of Impact Engineering 36.1: 61-72.

Zia, Asad, Pu Zhang, and Ivan Holly. (2023). “Long-term performance of concrete reinforced with scrap tire steel fibers in hybrid and non-hybrid forms: Experimental behavior and practical applications.” Construction and Building Materials 409: 134011.